Modeling and experiment of three-degree-of-freedom actuators using piezoelectric buzzers

2013 Smart Mater. Struct. 22 105006

(http://iopscience.iop.org/0964-1726/22/10/105006)

Smart Mater. Struct. **22** (2013) 105006 (10pp) doi:10.1088/0964-1726/22/10/105006

Modeling and experiment of three-degree-of-freedom actuators using piezoelectric buzzers

W M Chen and T S Liu

Department of Mechanical Engineering, National Chiao Tung University, Hsinchu 30010, Taiwan, Republic of China

E-mail: tsliu@mail.nctu.edu.tw

Received 17 June 2013
Published 29 August 2013
Online at stacks.iop.org/SMS/22/105006

Abstract

This study presents innovative three-degree-of-freedom piezoelectric actuators. Under the piezoelectric force and dry friction, the piezoelectric actuators not only can move in the Z-axis direction, but also rotate around the Y-axis and Z-axis. The Z-axis displacement can reach 62 mm and the rotation angle around the Y-axis and Z-axis can reach 270° and 360°, respectively. Compared with the literature, this innovative actuator design achieves one-degree-of-freedom translation and two-degree-of-freedom rotation. Equations of motion are derived based on the piezoelectric properties and Newton's law. Two types of actuators are created in this study. In the first type, the centers of four piezoelectric buzzers are attached to an arm while in the other type each rim of the four piezoelectric buzzers is attached to the arm. Experimental results are compared with theoretical results. According to the experimental results, the present actuator can accomplish a translational velocity of 11 mm s^{-1}, a Y-axis angular velocity of 8.96 rad s^{-1}, a Z-axis angular velocity of 2.63 rad s^{-1}, and a force of 2.49 mN. By using four piezoelectric buzzers, this study creates piezoelectric actuators capable of both translational and rotational motions.

(Some figures may appear in colour only in the online journal)

1. Introduction

With the development of science and technology in various technical fields, such as aerospace, optics, electronics, and medical engineering, high-precision actuators are required [1–6]. Based on the driving principles, the types of precision actuators include electrostrictive, magnetostrictive, artificial muscle actuators, shape memory alloy, photostrictive, and mechanochemical actuators. In the electrostrictive category, piezoelectric actuators are small and possess nanoscale displacement resolution and large driving forces [7].

The piezoelectric material used in an actuator comes in various types: multilayer, unimorph, bimorph, cylindrical, ring, and disk forms [8–10]. By means of an impact drive force, moving bodies can be driven by the impulse force [11–13] or by alternate stick and slip method [14–20]. Piezoelectric actuators are employed in precision platforms, atomic force microscopes (AFM) [21], mobile phones, and digital camera lens drives. To achieve innovative and diverse actuator applications, this study is focused on actuators with three degrees of freedom (DOF), for which four piezoelectric buzzers subjected to both a piezoelectric force and dry friction are employed to undergo Z-axis displacement as well as Y-axis and Z-axis rotations. Compared with the literature, this innovative piezoelectric actuator design can achieve 1-DOF translation and 2-DOF rotation. The piezoelectric buzzers play the role as a driving source in this actuator. Under appropriate combinations of the driving voltage and the duty ratio, the piezoelectric buzzers generate different piezoelectric forces and deformation velocities, finally producing a displacement of the moving body. Actuator characteristics, including the velocity, angular velocity, and force are measured to validate the theoretical models.

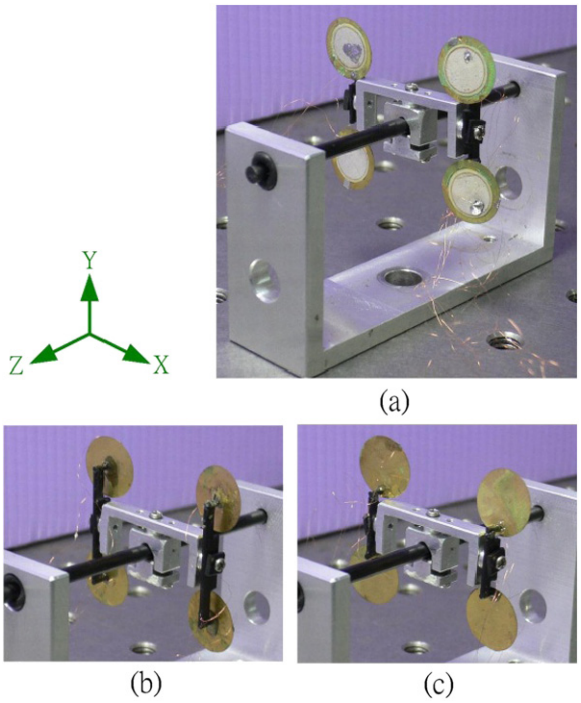

Figure 1. (a) Photo of the present piezoelectric actuator in the front view with two types: (b) type-A in the back view, whose piezoelectric buzzers are attached to the arm at the buzzer centers, and (c) type-B in the back view, whose piezoelectric buzzers are attached to the arm at the buzzer rims.

Future applications of the 3-DOF piezoelectric actuators proposed in this study include mobile phone cameras, digital cameras, digital video cameras, and atomic force microscopes. The current digital products on the market carry out automatic focusing and optical zooming in only one coordinate axis. By contrast, the advantage of employing the proposed 3-DOF piezoelectric actuator is that it can directly adjust two angles of the optical lens in addition to focusing or zooming along a coordinate axis. This feature becomes desirable concerning compact products.

2. Three-DOF piezoelectric actuator design and driving process

As depicted in figure 1, this study has designed and fabricated two types of actuators: in type-A, four piezoelectric buzzers are fixed at their center points, while in type-B four piezoelectric buzzers are fixed at the buzzer rims. Hence, the only difference between both designs lies in the fixed point positions that are glued to the arms. Dealing with buzzers of disk geometry, both designs represent the largest difference in boundary conditions, one fixed at the disk center and the other at the disk rim. This is the reason why this study chooses types A and B. However, it was not known which design performed better until experiments were carried out.

Figure 2 shows that the proposed actuator moves in three DOFs, for which red arrows in figure 2 represent the directions of displacement and rotations. The actuator consists of a moving body, a rod, and a base. As depicted in figure 3,

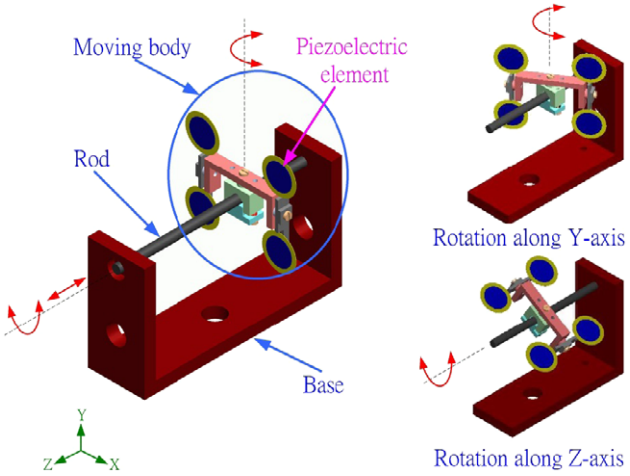

Figure 2. Three-DOF piezoelectric actuator moving on a rod or rotating around the *Y* or *Z* axes. Red arrows represent the directions of displacement and rotations of the moving body.

the moving body comprises a bracket, an upper part, a lower part, two driving parts, five screws, and five springs. The driving part consists of two piezoelectric buzzers and an arm. Figure 3 shows an exploded view of the 3-DOF actuator and the dimensions of the two driving part types. The diameter and length of the rod are 3 mm and 70 mm, respectively. The rod and arm are made from carbon fiber material. The bracket, upper part, lower part, and base are made from aluminum alloy. The moving body masses of types A and B are 2538 mg and 2481 mg, respectively. Screws between the moving body and the rod are adjusted in order to generate appropriate preloads and dry friction so as to expedite movement. Springs are used on the moving body to maintain a set value for preload and friction. The advantages of carbon fiber materials include light weight and a low coefficient of friction. The piezoelectric actuator selects carbon fiber as the rod material, because the coefficient of kinetic friction of carbon fiber is lower than metal and leads to a higher velocity between the rod and the moving body; thus, the moving body easily moves through a long displacement. For the arm, fiber carbon is selected due to its light weight.

The piezoelectric buzzers play the role of a driving source in this innovative piezoelectric actuator. A positive voltage causes a shrinking deformation in the piezoelectric buzzer, while a negative voltage causes an expansion. The deformation speed of the piezoelectric buzzer is adjusted by the duty ratio. Figure 4 depicts the principle of actuator translation motion along the *Z*-axis direction. The driving process is as follows: (a) the moving body is initially stationary. (b) When the four piezoelectric buzzers deform slowly, the piezoelectric force is smaller than the force of dry friction; thus, the moving body does not produce motion and remains in its original location. (c) When the four piezoelectric buzzers deform rapidly, the piezoelectric force becomes greater than the friction and triggers motion of the moving body, which moves along the *Z*-axis direction. (d) Finally, the four piezoelectric buzzers return to their undeformed state. When steps (a)–(d) are repeated, the

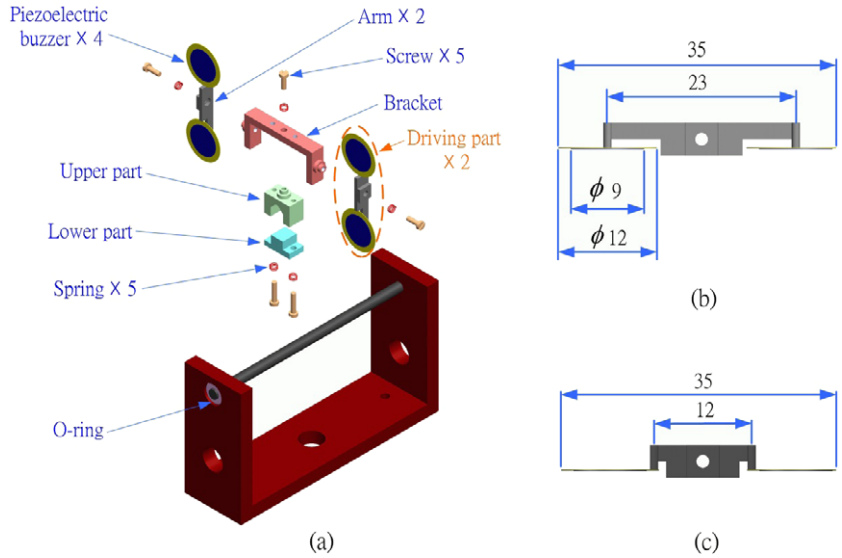

Figure 3. Exploded view of a 3-DOF piezoelectric actuator and the dimensions of the driving part: (a) exploded view; (b) driving part dimensions in mm of the type-A actuator; and (c) driving part dimensions in mm of the type-B actuator.

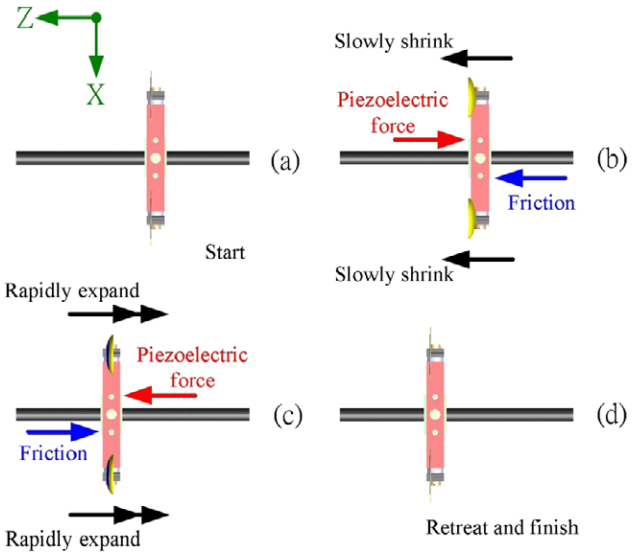

Figure 4. Principle of actuator translation: (a) the moving body is initially stationary. (b) When four piezoelectric buzzers shrink slowly, the moving body does not produce motion and remains in its original location. (c) When the piezoelectric buzzers expand rapidly, the piezoelectric force triggers motion of the moving body. (d) The four buzzers return to their undeformed state.

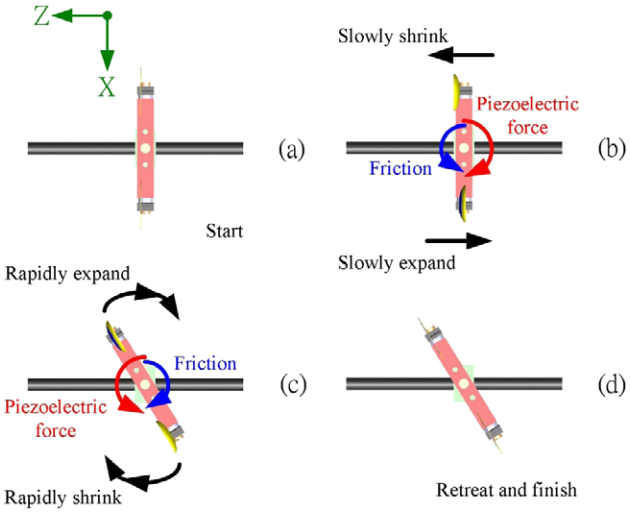

Figure 5. Principle of actuator rotation motion: (a) the moving body is initially stationary. (b) When the top buzzers shrink slowly while the bottom buzzers expand slowly, the piezoelectric force is too small to move the moving body. (c) When the top buzzers expand rapidly while the bottom buzzers shrink rapidly, the generated torque enables the moving body to rotate counterclockwise. (d) Finally, the four piezoelectric buzzers return to their undeformed state.

moving body continues to move in the *Z*-axis direction. Conversely, if the four piezoelectric buzzers first shrink rapidly shrink before they expand slowly, the moving body moves in the opposite direction.

Figure 5 shows the principle of actuator rotation motion around the *Y*-axis. The axis of the piezoelectric buzzers is parallel to the rod. The principle is described as follows: (a) the moving body is initially stationary. (b) When the top buzzers shrink slowly while the bottom buzzers expand slowly, the piezoelectric force is too small to move the moving body and there is no motion or angle rotation. (c) When the top buzzers expand rapidly while the bottom buzzers shrink rapidly, the generated torque due to four piezoelectric forces in opposite directions enables the moving body to rotate counterclockwise. Conversely, if the top buzzers shrink rapidly while the bottom buzzers expand rapidly, the generated torque due to the four piezoelectric forces in opposite directions enables the moving body to rotate clockwise. (d) Finally, the four piezoelectric buzzers return to their undeformed state. When steps (a)–(d) are repeated, the moving body continues to rotate counterclockwise.

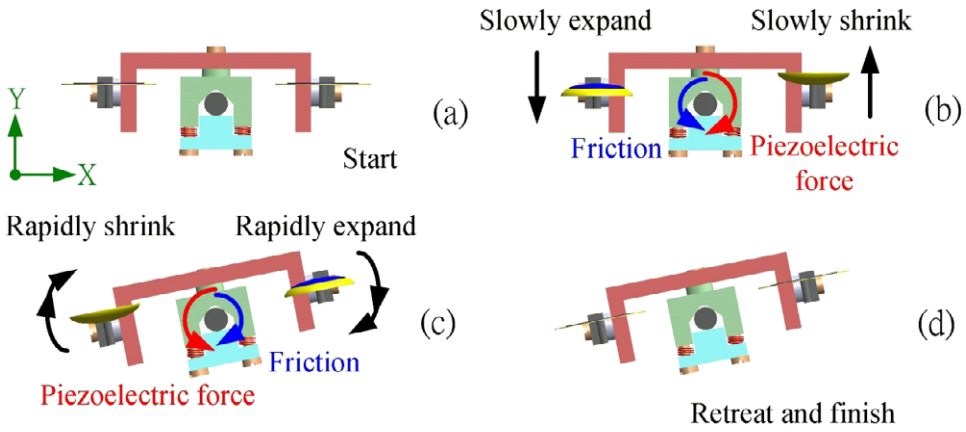

Figure 6. Principle of actuator rotation motion: (a) the moving body is initially stationary. (b) When the right buzzers shrink slowly while the left buzzers expand slowly, the piezoelectric force is too small to move the moving body. (c) When the right buzzers expand rapidly while the left buzzers shrink rapidly, the generated torque enables the moving body to rotate counterclockwise. (d) Finally, the four piezoelectric buzzers return to their undeformed state.

Figure 6 shows the principle of actuator rotation motion around the *Z*-axis. The axis of the piezoelectric buzzers is perpendicular to the rod. The principle is described as follows: (a) the moving body is initially stationary. (b) When the right buzzers shrink slowly while the left buzzers expand slowly, the piezoelectric force is too small to move the moving body, and the moving body does not produce motion or angle rotation. (c) When the right buzzers expand rapidly while the left buzzers shrink rapidly, the generated torque due to the four piezoelectric forces in opposite directions enables the moving body to rotate counterclockwise. Conversely, if the right buzzers shrink rapidly while the left buzzers expand rapidly, the generated torque due to the four piezoelectric forces in opposite directions enables the moving body to rotate clockwise. (d) Finally, the four piezoelectric buzzers return to their undeformed state. When steps (a)–(d) are repeated, the moving body continues to rotate counterclockwise.

3. Theoretical derivation

This paper presents actuators of two types: type-A, whose piezoelectric buzzers are attached to an arm at both buzzer centers, and type-B, whose piezoelectric buzzers are attached to the arm at the buzzer rims. It will be later described in another section on experiments that type-A moves faster than type-B. Therefore, this study only derives the dynamic equations of type-A. Based on the dynamic equations, this study calculates the piezoelectric forces and velocities of the moving body. These theoretical results are validated by experimental results.

Figure 7 shows the direction of both the driving voltage and the deformation of two buzzers. Figure 7(a) shows the buzzer state without the driving voltage. When two buzzers with both positive voltages travel in the same direction, two buzzers generate deformations and forces in the same direction. The principle enables the moving body to generate linear displacement, as shown in figure 7(b). However, as depicted in figure 7(c), if both buzzers with positive and negative voltages are traveling in opposite directions, the

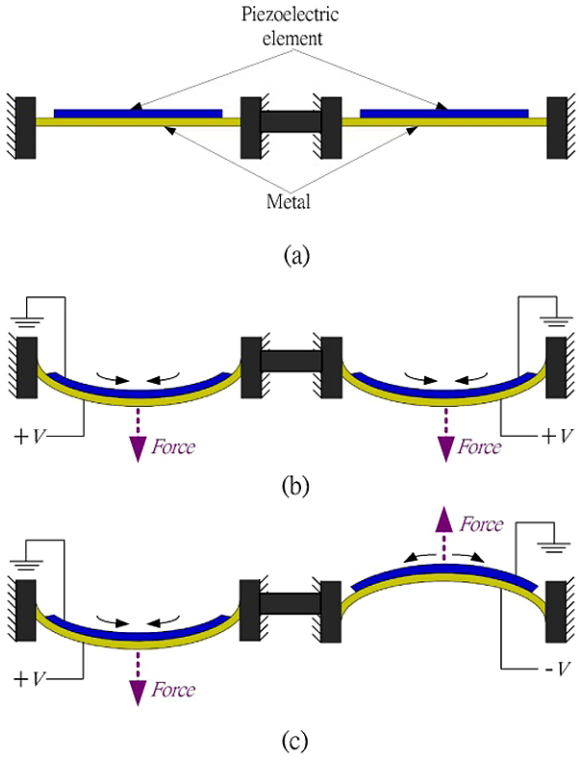

Figure 7. Driving voltage and deformation direction of two piezoelectric buzzers: (a) subject to zero voltage; (b) both subject to positive voltages; and (c) subject to positive and negative voltages, respectively.

both buzzers generate deformations and forces in opposite directions, which cause the moving body shown in figure 5(c) to rotate.

Assuming that the rim of a piezoelectric buzzer is fixed but the center can vibrate freely. When the driving voltage is applied to the buzzer, the buzzer center deforms. The mechanical model of the proposed piezoelectric actuators is depicted in figure 8. As the voltage is applied to the piezoelectric buzzers, they rapidly produce deformation,

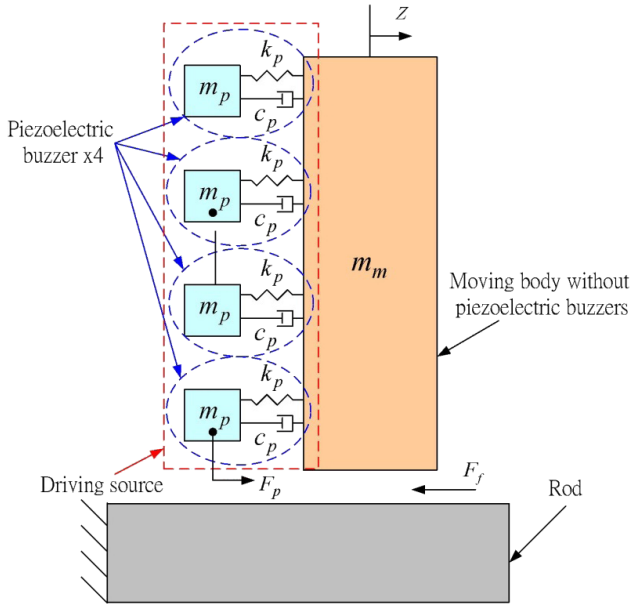

Figure 8. Mechanical model of the present piezoelectric actuator.

producing a force to the right. In the presence of dynamic friction between the rod and the moving body, the moving body moves to the right. Subjected to four piezoelectric forces F_p generated by the four buzzers and the friction force F_f, employing Newton's second law leads to the dynamic equation

$$\left(4m_\mathrm{p} + m_\mathrm{m}\right)\ddot{z} + 4c_\mathrm{p}\dot{z} + 4k_\mathrm{p}z = 4F_\mathrm{p} - F_\mathrm{f} \tag{1}$$

where m_p is the buzzer mass, m_m is the mass of the moving body excluding the buzzers, c_p is the damping coefficient of the piezoelectric buzzer, k_p is the stiffness coefficient of the piezoelectric buzzer, $\ddot{z}$ is the moving body acceleration, $\dot{z}$ is the moving body velocity, and z is the moving body displacement.

If a concentrated loading P is applied to the buzzer disk center, the shear force Q_r at the disk rim and the loading P are equal but in opposite directions. Hence,

$$2\pi r Q_\mathrm{r} = -P \tag{2}$$

where the shear force is expressed by [22]

$$Q_\mathrm{r} = -D\frac{\mathrm{d}}{\mathrm{d}r}(\nabla^2\omega) = -D\frac{\mathrm{d}}{\mathrm{d}r}\left(\frac{\mathrm{d}^2\omega}{\mathrm{d}r^2} + \frac{1}{r}\frac{\mathrm{d}\omega}{\mathrm{d}r} + \frac{1}{r^2}\frac{\mathrm{d}^2\omega}{\mathrm{d}\theta^2}\right) \tag{3}$$

where ω denotes the buzzer deformation in the axial direction and D the bending stiffness. Substituting equation (3) into (2) gives

$$\frac{\mathrm{d}}{\mathrm{d}r}(\nabla^2\omega) = \frac{\mathrm{d}}{\mathrm{d}r}\left(\frac{1}{r}\frac{\mathrm{d}}{\mathrm{d}r}r\frac{\mathrm{d}\omega}{\mathrm{d}r}\right) = -\frac{Q_\mathrm{r}}{D} = \frac{P}{2\pi rD}. \tag{4}$$

Integrating this equation three times gives

$$\omega = \frac{P}{8\pi D}(r^2\log r + Ar^2 + B\log r + C) \tag{5}$$

where A, B, and C are constants of integration. When the buzzer rim with radius a is fixed, the boundary conditions are

$$\begin{aligned} \frac{\mathrm{d}\omega}{\mathrm{d}r} &= 0, \qquad \text{when } r = 0 \\ \omega &= \frac{\mathrm{d}\omega}{\mathrm{d}r} = 0, \qquad \text{when } r = a. \end{aligned} \tag{6}$$

Substituting equation (5) into (6) yields the unknown constants

$$A = -\tfrac{1}{2} - \log a, \qquad B = 0, \qquad C = \tfrac{1}{2}a^2. \tag{7}$$

Substituting equation (7) into (5) yields the buzzer deformation

$$\omega = \frac{P}{8\pi D}\left[\frac{1}{2}(a^2 - r^2) + r^2\log\frac{r}{a}\right]. \tag{8}$$

The radial moment M_r and the tangential moment M_θ are respectively written as [22]

$$\begin{aligned} M_\mathrm{r} &= -D\left(\frac{\mathrm{d}^2\omega}{\mathrm{d}r^2} + \frac{\nu}{r}\frac{\mathrm{d}\omega}{\mathrm{d}r}\right) \\ M_\theta &= -D\left(\frac{1}{r}\frac{\mathrm{d}\omega}{\mathrm{d}r} + \nu\frac{\mathrm{d}^2\omega}{\mathrm{d}r^2}\right) \end{aligned} \tag{9}$$

where ν is the Poisson's ratio. Substituting equation (8) into (9) gives the moments

$$\begin{aligned} M_\mathrm{r} &= \frac{P}{4\pi}\left[(1+\nu)\log\frac{a}{r} - 1\right] \\ M_\theta &= \frac{P}{4\pi}\left[(1+\nu)\log\frac{a}{r} - \nu\right]. \end{aligned} \tag{10}$$

The radial stress σ_r and the tangential stress σ_θ are respectively written as [22]

$$\begin{aligned} \sigma_\mathrm{r} &= -\frac{6M_\mathrm{r}}{t^2} \\ \sigma_\theta &= -\frac{6M_\theta}{t^2} \end{aligned} \tag{11}$$

where t is the thickness. Substituting equations (10) into (11) yields the stresses

$$\begin{aligned} \sigma_\mathrm{r} &= \frac{-6P}{4\pi t^2}\left[(1+\nu)\log\frac{a}{r} - 1\right] \\ \sigma_\theta &= \frac{-6P}{4\pi t^2}\left[(1+\nu)\log\frac{a}{r} - \nu\right]. \end{aligned} \tag{12}$$

According to Hooke's law, the radial strain ε_r and the tangential strain ε_θ are respectively written as

$$\begin{aligned} \varepsilon_\mathrm{r} &= \frac{1}{E}\left(\sigma_\mathrm{r} - \nu\sigma_\theta\right) \\ \varepsilon_\theta &= \frac{1}{E}\left(\sigma_\theta - \nu\sigma_\mathrm{r}\right). \end{aligned} \tag{13}$$

Substituting equations (12) into (13) gives

$$\begin{aligned} \varepsilon_\mathrm{r} &= \frac{-6P}{4\pi Et^2}\left[(1+\nu)(1-\nu)\log\frac{a}{r} - (1-\nu^2)\right] \\ \varepsilon_\theta &= \frac{-6P}{4\pi Et^2}\left[(1+\nu)(1-\nu)\log\frac{a}{r}\right]. \end{aligned} \tag{14}$$

Dealing with circular plates, the piezoelectric equation can be written as [23]

$$\varepsilon_\mathrm{r} = s_{11}^\mathrm{E}\sigma_\mathrm{r} + s_{12}^\mathrm{E}\sigma_\theta + s_{13}^\mathrm{E}\sigma_z + d_{31}E_z \tag{15}$$

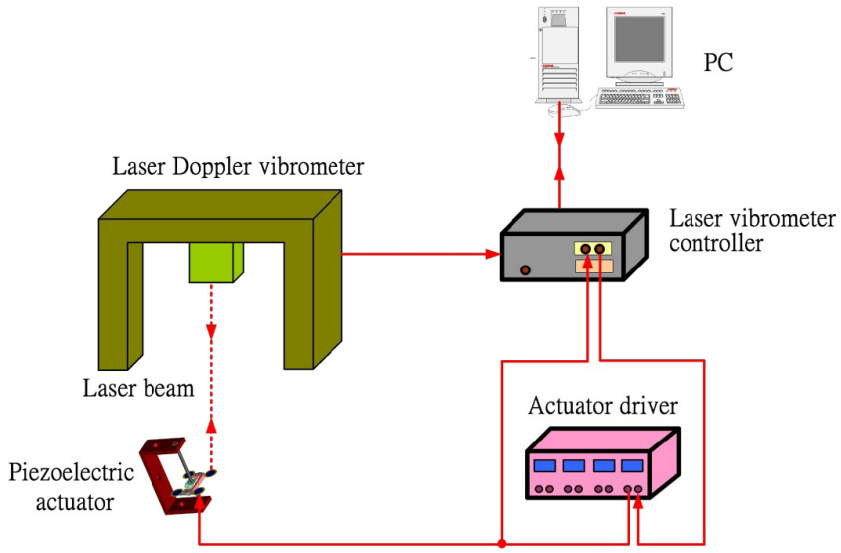

Figure 9. Experimental setup for actuator system identification.

where $s_{11}^{\mathrm{E}}, s_{12}^{\mathrm{E}}$, and s_{13}^{E} denote the elasticity constants of the piezoelectric buzzer, d_{31} the charge constant of the piezoelectric buzzer, σ_z the axial stress, and E_z the exerted electric field. The piezoelectric force and the electric field are respectively written as [24]

$$F_{\mathrm{p}} = \sigma_z A_1 \tag{16}$$

$$E_z = \frac{V}{t} \tag{17}$$

where A_1 denotes the buzzer disk area and V the exerted electric voltage. Substituting equations (12), (14), (16) and (17) into (15) yields the piezoelectric force

$$F_{\mathrm{p}} = \frac{A_1}{S_{13}^{\mathrm{E}}}\left(\varepsilon_{\mathrm{r}} - s_{11}^{\mathrm{E}}\sigma_{\mathrm{r}} - s_{12}^{\mathrm{E}}\sigma_\theta - d_{31}\frac{V}{t}\right). \tag{18}$$

The friction force between the moving body and rod can be expressed by [25]

$$F_{\mathrm{f}}(\dot{z}) = \gamma_1\left(\tanh\left(\gamma_2\dot{z}\right) - \tanh\left(\gamma_3\dot{z}\right)\right) + \gamma_4\tanh\left(\gamma_5\dot{z}\right) + \gamma_6\dot{z}. \tag{19}$$

Based on equation (19), the static friction coefficient can be approximated by $\gamma_1 + \gamma_4$. The term $\tanh(\gamma_2\dot{z}) - \tanh(\gamma_3\dot{z})$ captures the Stribeck effect, where the friction coefficient decreases from the static friction coefficient with increasing slip velocity. The third term $\gamma_4\tanh(\gamma_5\dot{z})$ accounts for the Coulomb friction effect. The last term $\gamma_6\dot{z}$ accounts for the viscous dissipation effect. Finally, substituting equations (18) and (19) into (1) yields the dynamic equation. Table 1 lists the parameters used in the simulation.

Table 1. Material parameters of the actuator.

$m_{\mathrm{p}} = 6.5 \times 10^{-5}$ kg	$m_{\mathrm{m}} = 1.285 \times 10^{-3}$ kg
$c_{\mathrm{p}} = 23.45$ N s m^{-1}	$k_{\mathrm{p}} = 5 \times 10^{6}$ N m^{-1}
$s_{11}^{\mathrm{E}} = 1.23 \times 10^{-11}$ m^2 N^{-1}	$s_{12}^{\mathrm{E}} = -4.05 \times 10^{-12}$ m^2 N^{-1}
$s_{13}^{\mathrm{E}} = -5.31 \times 10^{-12}$ m^2 N^{-1}	$d_{31} = -1.23 \times 10^{-10}$ cl N^{-1}
$t = 1.3 \times 10^{-4}$ m	$r = 6 \times 10^{-3}$ m
$E = 2.216 \times 10^{10}$ N m^{-2}	$\nu = 0.33$
$A_1 = 1.13 \times 10^{-4}$ m^2	$P = 1 \times 10^{-5}$ kg
$\gamma_1 = 0.25$	$\gamma_2 = 100$
$\gamma_3 = 10$	$\gamma_4 = 0.1$
$\gamma_5 = 100$	$\gamma_6 = 0.001$

4. Experimental results and discussion

4.1. System identification

System identification is conducted to investigate the piezoelectric buzzer characteristics and identify resonance frequencies before selecting a resonant frequency for driving the moving body. Exciting buzzers at the resonance frequency enables the moving body to move at high speeds. Figure 9 shows the experimental setup for system identification, for which the output is buzzer deformation and the input is a sinusoidal driving voltage of 2V in the scanning range from 10 and 20 kHz. The driving voltage of the actuator driver is adjusted to drive the moving body on the piezoelectric actuator. The vibrometer emits laser beams to measure buzzer deformation, passing the signal value of the vibratory deformation to the vibrometer controller. Finally, vibration data stored in the vibrometer controller are converted into Bode diagrams. Corresponding to figure 1, which shows photographs of type A and B actuators, figure 10 depicts their Bode diagrams, where the resonance frequencies of type-A include 3036, 3377, and 7445 Hz and those of type-B are 396, 536, and 6900 Hz. Accordingly, type-A has a larger bandwidth than type-B.

4.2. Performance measurement

Velocity measurement, angular velocity measurement, and force measurement experiments are carried out for comparison between actuators of types A and B. According

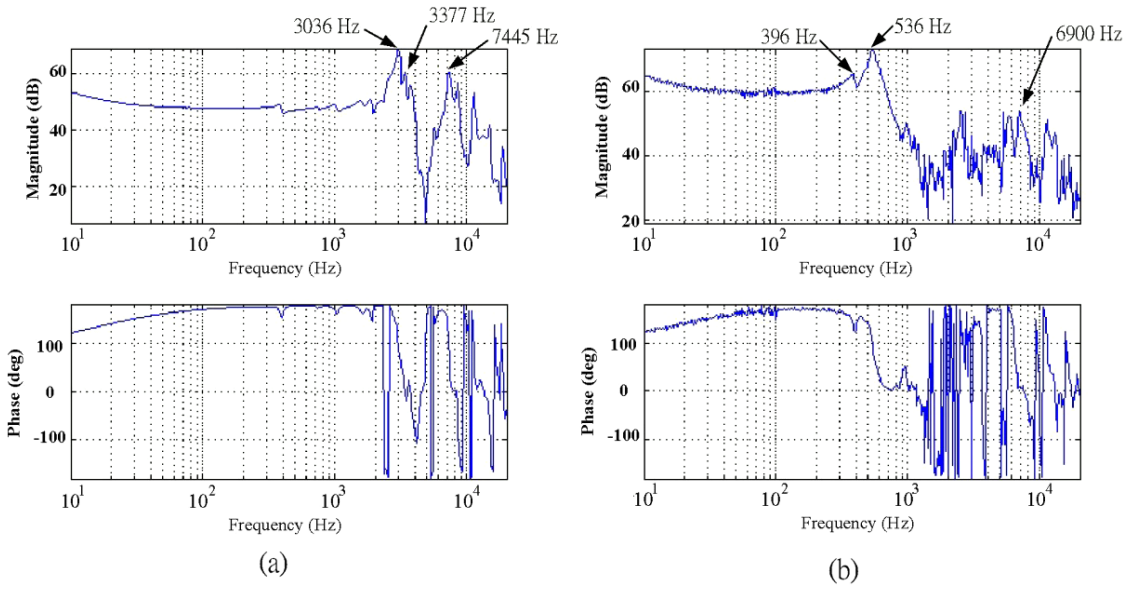

Figure 10. Bode diagrams of (a) type-A and (b) type-B actuators.

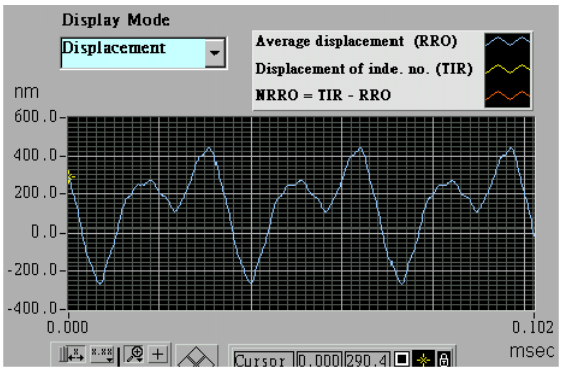

Figure 11. Measured deformation of a piezoelectric buzzer subjected to square wave input voltage.

to the resonant peaks, the driving frequencies selected for both actuators are 3036 Hz and 6900 Hz, respectively. When the driving voltage employs square waves [17, 18] to drive the piezoelectric buzzer, according to the excitation frequency, frequency response of the piezoelectric buzzer, and duty ratio of the driving voltage, the piezoelectric buzzer deforms, as depicted in figure 11. Changes in the duty ratio influence the movement direction and velocity. Figure 11 shows the measured buzzer deformation. For the actuator velocity measurement, figure 12 shows the experimental setup, which includes a vibrometer controller (Polytec OFV 3001), vibrometer (Polytec OFV 512), waveform generator (Agilent 33210A), and actuator driver (Echo ENP-4012B). In experiments, firstly, the waveform generator is used to generate the square voltage waveform with a duty ratio. The driving voltage of the actuator driver is adjusted so as to drive the actuators. The vibrometer is used to measure the actuator displacement and velocity, which are in turn transmitted to the vibrometer controller.

The difference of force measurement and velocity measurement lies in an equipment change, from the vibrometer to a precise electronic scale. For the actuator force measurement, figure 13 shows the experimental setup, which includes a waveform generator (Agilent 33210A), an actuator driver (Echo ENP-4012B), and a precise electronic scale (Precisa XS 625M) with 0.01 mN resolution. Buzzers generate tiny forces due to the $t = 0.8$ mm thickness in the piezoelectric film. In order to effectively measure the actuator force resultant from the buzzers, this study uses the scale to replace force sensors whose resolution is 1 mN only. In experiments, firstly, the waveform generator is used to generate a square waveform with a duty ratio. The driving voltage of the actuator driver is adjusted so as to drive the actuator. As depicted in the upper left part of figure 13, point a on the moving body is located at the geometric center of the four buzzers. A carbon fiber rod connects point a on the moving body and the scale center. When the actuator exerts force via the carbon fiber rod to the scale center, the scale is able to measure the resultant force of the four buzzers.

Under appropriate combinations of the driving voltage and the duty ratio, the piezoelectric buzzers generate different piezoelectric forces and deformation velocities, finally producing the displacement of the moving body. Experimental and simulation results of the velocity variation with duty ratios are depicted in figure 14, in which the driving voltage is 40 V for both actuators and the driving frequencies are 3036 Hz and 6900 Hz for types A and B, respectively. When the duty ratio is prescribed as 50%, the buzzer deforms in an isosceles triangle waveform and the velocity of the moving body is difficult to control and stabilize; thus, a duty ratio of 50% is not appropriate. According to experiments, 10% and 90% duty ratios have little effect on the velocity; thus, the results of both duty ratios are not included in comparison. Figure 14 also shows that when the duty ratio is 20%–40% and 60%–80%, the moving bodies moved in opposite directions. The fastest speed is obtained at duty ratios of 40% and 60%. The type-A actuator moves faster

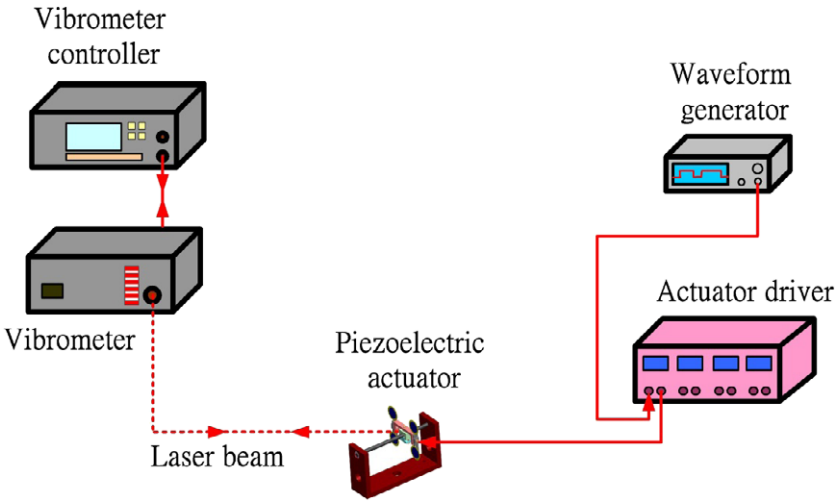

Figure 12. Experimental setup for the actuator velocity measurement.

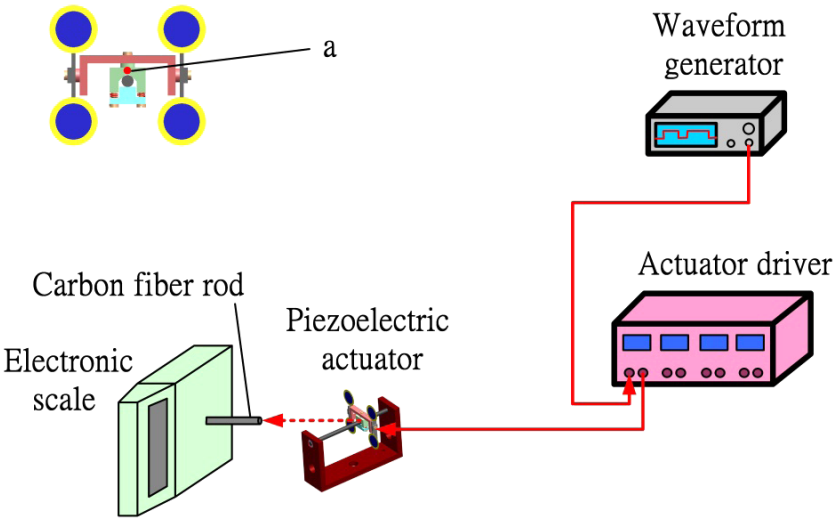

Figure 13. Experimental setup for the actuator force measurement. For the purpose of measuring forces coming from all four buzzers, the end of the carbon fiber rod is glued to touch point a, which is located at the geometric center of the moving body.

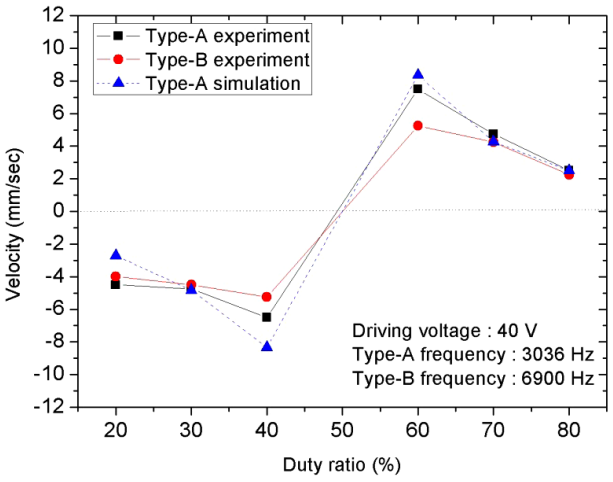

Figure 14. Comparison of the experimental and simulation results for velocity variation with the duty ratios.

than type-B actuator. Type-A simulation results are only slight variations from experimental results of type-A since the equations of motion are derived based on the type-A geometry.

Figure 15 shows that the moving velocity is proportional to the driving voltage. The type-A actuator moves significantly faster than the type-B actuator. Moreover, the moving velocity of type-A and type-B experiments under a driving voltage of 50 V can reach 11 mm s^{-1} and 8 mm s^{-1}, respectively. The moving velocity of the type-A simulation under a driving voltage of 50 V is 10.7 mm s^{-1}. The maximum distance traveled in the Z-axis direction is 62 mm. If there is no space constraint, the distances traveled by the moving bodies are unlimited.

Concerning the Y-axis rotational motion of the actuators, figure 16 shows that the angular velocity increases with the drive voltage. In addition, the measured angular velocity of type-A is faster than type-B. The angular

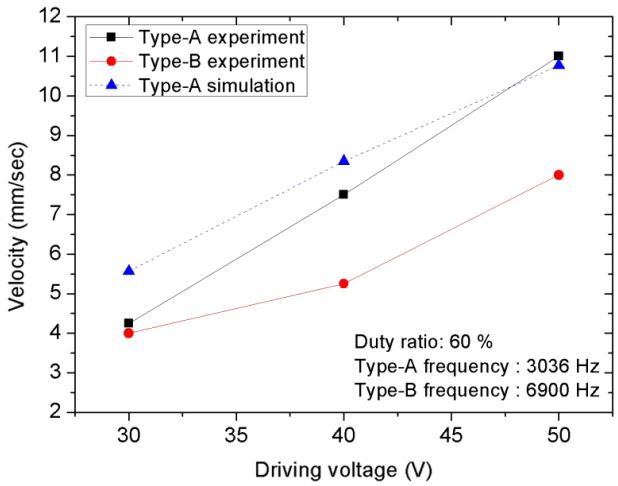

Figure 15. Comparison of experimental and simulation results in the translational velocity.

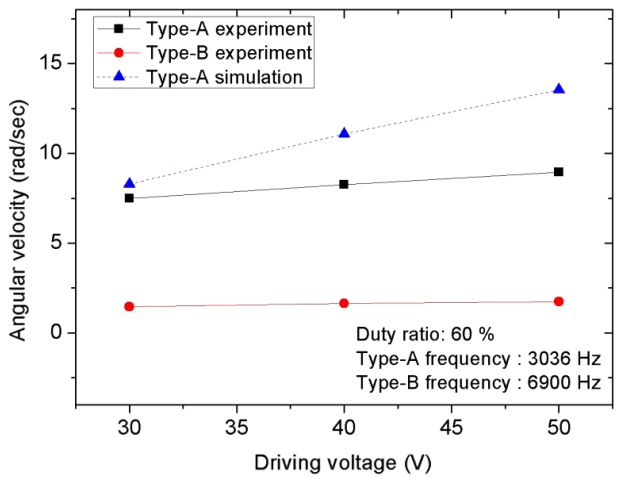

Figure 16. Comparison of experimental and simulation results for the *Y*-axis angular velocity.

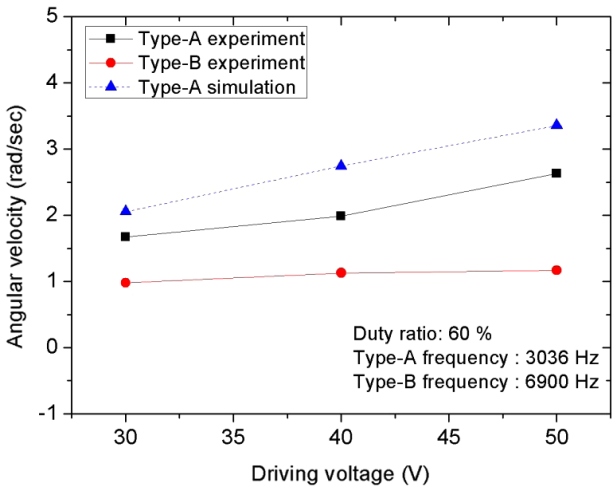

Figure 17. Comparison of experimental and simulation results for the *Z*-axis angular velocity.

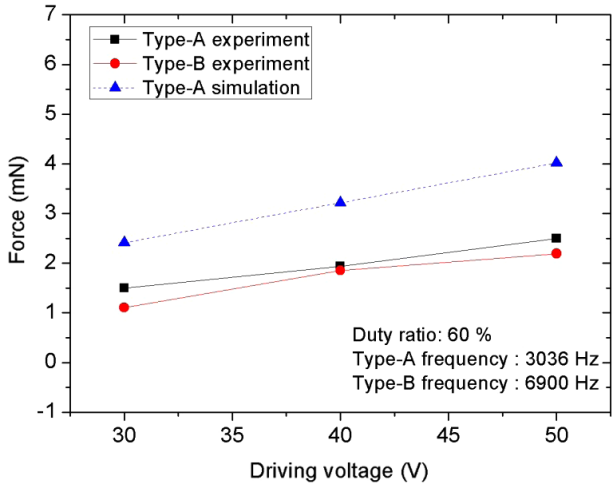

Figure 18. Comparison of experimental and simulation results of the actuator force along the rod versus the voltage.

velocities of type-A and type-B experiments under a driving voltage of 50 V are 8.96 rad s^{-1} and 1.74 rad s^{-1}, respectively. The angular velocity of type-A simulation under a driving voltage of 50 V is calculated as 13.54 rad s^{-1}. Unbalanced weights on both sides of the rotational arm, as shown in figure 3(a), result in an angular velocity discrepancy between simulation and experimental results. The maximum rotation angle in the *Y*-axis direction, which is depicted in figures 1 and 2, can reach 270° in experiments.

Concerning the *Z*-axis rotational motion of the actuators, figure 17 shows that the angular velocity increases with the drive voltage. In addition, the measured angular velocity of type-A is faster than type-B. The angular velocities of type-A and type-B experiments under a driving voltage of 50 V are 2.63 rad s^{-1} and 1.17 rad s^{-1}, respectively. The angular velocity of the type-A simulation under a driving voltage of 50 V is 3.35 rad s^{-1}. The measured angular velocities of 50 V are smaller than the calculated angular velocities in the simulation results due to unbalanced weights at both sides of the bracket and the gravitational acceleration of the bracket. The maximum rotational angle in the *Z*-axis direction, which is depicted in figures 1 and 2, can reach 360° in experiments.

Figure 18 shows that the actuator force is proportional to the driving voltage. The force of the type-A and type-B experiments under a driving voltage of 50 V can reach 2.49 mN and 2.19 mN, respectively. The force of the type-A simulation under a driving voltage of 50 V is 4.01 mN. According to figure 18, actuator forces increase with the driving voltage. The measured force from the type-A actuator is larger than from the type-B actuator. The measured forces are smaller than the calculated forces in the simulation results due to the unbalanced weights and inertial force at both sides of the bracket. According to the overall comparison, type-A is superior to type-B, which is attributed to the fact that type-A is pasted at its center with the arm and hence generates larger forces and velocity while type-B is pasted at its rim.

5. Conclusion

This study has constructed a model and carried out experiments for innovative 3-DOF piezoelectric actuators, alternately subjected to a piezoelectric force and dry friction, which not only are capable of translation but also rotation. Compared with the literature, the present new piezoelectric actuator design achieves both 1-DOF translational and 2-DOF rotational motions. Experimental results depict that the present actuator can accomplish a translational velocity of 11 mm s^{-1}, an Y-axis angular velocity of 8.96 rad s^{-1}, an Z-axis angular velocity of 2.63 rad s^{-1}, and 2.49 mN in force. According to the experimental results concerning velocities, angular velocities and forces, type-A performs better than type-B because the type-A design leads to larger forces and a faster velocity. The derived dynamic model that incorporates both mechanical and piezoelectric properties is validated by experimental results.

References

[1] Watson B, Friend J and Yeo L 2009 Piezoelectric ultrasonic micro/milli-scale actuators *Sensors Actuators* A **152** 219–33

[2] Wang C-K, Huang H-P and Chien K 2008 Piezo-electric driver of ultrasonic motor on the humanoid robot *IEEE Advanced Robotics and its Social Impacts* pp 23–5

[3] Uchino K 2007 Piezoelectric actuators 2006 *J. Electroceram.* **20** 1–11

[4] Bansevicius R and Blechertas V 2007 Multi-degree-of-freedom ultrasonic motors for mass-consumer devices *J. Electroceram.* **20** 1–4

[5] Morita T 2003 Miniature piezoelectric motors *Sensors Actuators* A **103** 291–300

[6] Zhang Z M, An Q, Li J W and Zhang W J 2012 Piezoelectric friction-inertia actuator—a critical review and future perspective *Int. J. Adv. Manuf. Technol.* **62** 1–17

[7] Uchino K and Giniewicz J R 2003 *Micromechatronics* (New York: Dekker) pp 3–7

[8] Liu P-K, Wen Z-J and Sun L-N 2009 An in-pipe micro robot actuated by piezoelectric *Chin. Sci. Bull.* **54** 2134–42

[9] Sun D, Wang S, Sakurai J, Choi K-B, Shimokohbe A and Hata S 2010 A piezoelectric linear ultrasonic motor with the structure of a circular cylindrical stator and slider *Smart Mater. Struct.* **19** 1–9

[10] Yan S, Zhang F, Qin Z and Wen S 2006 A 3-DOFs mobile robot driven by a piezoelectric actuator *Smart Mater. Struct.* **15** 7–13

[11] Mazeika D and Vasiljev P 2013 Linear inertial piezoelectric motor with bimorph disc *Mech. Syst. Signal Process.* **36** 1–8

[12] Kawakita S, Isogai T, Ohya N and Kawahara N 1997 Multi-layered piezoelectric bimorph actuator *IEEE Int. Symp. on Micromechatronics and Human Science* pp 73–8

[13] Zhang H-Z, Cheng G-M, Zhao H-W, Zeng P and Yang Z-G 2006 A 2-dimensional impact driven precise actuator using piezoelectric bimorphs *Front. Electr. Electron. Eng. China* **4** 405–9

[14] Ko H-P, Lee K-J, Yoo K-H, Kang C-Y, Kim S and Yoon S-J 2006 Analysis of tiny piezoelectric ultrasonic linear motor *Japan. J. Appl. Phys.* **45** 4782–6

[15] Ko H-P, Kim S, Borodinas S N, Vasiljev P E, Kang C-Y and Yoon S-J 2006 A novel tiny ultrasonic linear motor using the radial mode of a bimorph *Sensor Actuators* A **125** 477–81

[16] Lim K-J, Lee J-S, Park S-H, Kang S-H and Kim H-H 2007 Fabrication and characteristics of impact type ultrasonic motor *J. Eur. Ceram. Soc.* **27** 4159–62

[17] Kang C-Y, Yoo K-H, Ko H-P, Kim H-J, Ko T-K and Yoon S-J 2006 Analysis of driving mechanism for tiny piezoelectric linear motor *J. Electroceram.* **17** 609–12

[18] Yoshida R, Okamoto Y and Okada H 2002 Development of smooth impact drive mechanism *Japan Soc. Precis. Eng.* **68** 536–41

[19] Morita T, Murakami H, Yokose T and Hosaka H 2012 A miniaturized resonant-type smooth impact drive mechanism actuator *Sensors Actuators* A **178** 188–92

[20] Nishimura T, Hosaka H and Morita T 2012 Resonant-type smooth impact drive mechanism (SIDM) actuator using a bolt-clamped langevin transducer *Ultrasonics* **52** 75–80

[21] Hunt J and Bhushan B 2012 Device level studies of adaptive optics sliding components in microprojectors *Microsyst. Technol.* **18** 137–48

[22] Timoshenko S and Woinowsky-Krieger S 1959 *Theory of Plates and Shells* (New York: McGraw-Hill) pp 51–72

[23] Zhang X Z, Veidt M and Kitipornchai S 2004 Transient bending of a piezoelectric circular plate *Int. J. Mech. Sci.* **46** 1845–59

[24] Deshpande M and Saggere L 2007 An analytical model and working equations for static deflections of a circular multi-layered diaphragm-type piezoelectric actuator *Sensors Actuators* A **136** 673–89

[25] Makkar C, Dixon W E, Sawyer W G and Hu G 2005 A new continuously differentiable friction model for control systems design *IEEE/ASME Int. Conf. on Advanced Intelligent Mechatronics* pp 600–5